Journal of Environmental Chemical Engineering 11 (2023) 110189

Contents lists available at ScienceDirect

Journal of Environmental Chemical Engineering

journal homepage: www.elsevier.com/locate/jece

Atomic-level analysis of migration and transformation of organic sodium in high-alkali coal pyrolysis using reactive molecular dynamics simulations

Cen Sun [a,b,c], Aixue Zhu [d], Tong Xu [a], Xiaolin Wei [b,c,*], Dikun Hong [a], Tong Si [e]

[a] Department of Power Engineering, North China Electric Power University, Baoding 071003, China
[b] State Key Laboratory of High-Temperature Gas Kinetics, Institute of Mechanics, Chinese Academy of Sciences, Beijing 100190, China
[c] School of Engineering Science, University of Chinese Academy of Sciences, Beijing 100049, China
[d] College of Chemistry & Environmental Science, Hebei University, Baoding 071002, China
[e] Key Laboratory for Thermal Science and Power Engineering of Ministry of Education, Department of Energy and Power Engineering, Tsinghua University, Beijing 100084, China

ARTICLE INFO

Editor: Javier Marugan

Keywords:
Inherent organic sodium
ReaxFF
Pyrolysis
Molecular simulation
Py-GC/MS

ABSTRACT

Monitoring the migration and transformation of free radicals and alkali metals (such as tar- and organic gas-bonded sodium) in high-alkali coal pyrolysis through experimental methods alone is a challenging task. To address this challenge, in this work we employed reactive force field (ReaxFF) molecular dynamics simulations to model the transformation behavior of sodium at the atomic level. The different forms of sodium [sodium atoms ($Na_{(g)}$), sodium hydroxide ($NaOH_{(g)}$), tar-bonded sodium, and organic gas-bonded sodium] were carefully analyzed to gain insights into their migration during the pyrolysis process. The results show that inherent organic sodium forms binary or multiple coordination structures with oxygen atoms in the coal matrix during pyrolysis. During pyrolysis, inherent organic sodium was transformed into three main sodium species: Na atoms, NaOH, and $Na{\cdot}H_2O$. The repeated reactions between these sodium-containing intermediates and the coal matrix strengthen the three-dimensional network structure of the coal matrix and hinder its graphitization. The preponderance of $Na_{(g)}$ predominantly stems from organic sodium $C_{1-40+}Na$, while NaOH and $Na{\cdot}H_2O$ contribute to a lesser extent. The formation of NaOH and $Na{\cdot}H_2O$ can be primarily attributed to the presence of $Na_{(g)}$, with merely a limited portion arising from organic sodium ($C_{1-40+}Na$). The results also show that organic sodium inhibits char and tar formation at high temperatures, whereas at low temperatures it promotes char formation and inhibits tar production.

1. Introduction

Alkali metals including sodium are a common occurrence in both coal and biomass fuels. They can deposit on thermal equipment and accelerate slagging and corrosion, posing a threat to the safe operation of the equipment. Thus, to promote the practical applications of high-sodium coal, it is imperative to study the migration and transformation characteristics of these alkali metals.

Glarborg and Marshall [1] described the detailed gaseous mechanism of alkali metal reactions (115 species, 1342 reactions) involving C/H/O/N/S/Cl/K/Na. The release process mechanism of the solid-phase alkali metal to the gas phase is helpful to provide the initial conditions for the reaction mechanism of gas-phase alkali metals. Regarding the release process of solid-phase alkali metals, previous investigations have mainly focused on macroscopic kinetic processes based on gas-phase alkali metals using in situ detection techniques [2–5]. Possible mechanisms involved part of the inorganic sodium being released through evaporation or dissociation (as shown in reaction A_1 in Table 1), with the other part being transformed into organic sodium (as shown in reactions A_2 and A_3 in Table 1). Organic sodium (such as R-COONa, R-ONa, and R-Na) might be further broken down to release gaseous sodium (as shown in reactions A_4–A_6 in Table 1).

The process of pyrolysis, driven by many coupled reaction pathways, is complex and involves numerous free radical reactions and intermediates. Online detection techniques can only monitor inorganic gaseous sodium species such as $NaCl_{(g)}$, sodium hydroxide ($NaOH_{(g)}$), or sodium atoms ($Na_{(g)}$). Monitoring the migration and transformation of free radicals and alkali metals in different forms (such as tar- and organic

* Corresponding author at: State Key Laboratory of High-Temperature Gas Kinetics, Institute of Mechanics, Chinese Academy of Sciences, Beijing 100190, China.
E-mail address: xlwei@imech.ac.cn (X. Wei).

https://doi.org/10.1016/j.jece.2023.110189
Received 12 February 2023; Received in revised form 21 May 2023; Accepted 22 May 2023
Available online 30 May 2023

Table 1
Migration and transformation path of sodium during thermal conversion.

Chemical reaction	Number	Ref.
$NaCl_{(s)} \rightarrow NaCl_{(g)}$	A_1	[6,7]
$NaCl(s)+Organic(s) \rightarrow Organic\text{-}Na(s) + HCl/CH_3Cl/tar\text{-}Cl$	A_2	[8–11]
$R\text{-}COOH+NaCl \rightarrow R\text{-}COONa+HCl$	A_3	[12]
$Organic - Na\ (R - COONa) \rightarrow CM - Na$	A_4	[13–15]
$Organic\text{-}Na\ (R\text{-}COONa) \rightarrow R+CO_2+Na_{(g)}$	A_5	[6,7,16]
$CM\text{-}Na \rightarrow Na_{(g)}$	A_6	[6,7]

gas-bonded sodium) is a challenging task. The limitations of experimental techniques complicate the deep exploration of the complex pyrolysis reaction pathways governing the volatilization of alkali metals from the solid to the gas phase.

Molecular simulations [17] can complement the experimental results. Most relevant investigations employing density functional theory (DFT) have used graphite-like layers as model compounds for coal molecules (the number of atoms in the system is less than 100) [18–24]. The addition of excess hydrogen atoms on the graphite-like layers alters the behavior of the carbon atoms. However, DFT simulations are only suitable for exploring the molecular configuration of small systems or local chemical reactions in macromolecular models.

In 2001, van Duin and Goddard [25] designed the reactive force field (ReaxFF) based on first-principles calculations, and extensive experiments. ReaxFF is a molecular dynamics method used for simulating chemical reactions. It is a powerful and flexible force field that can simulate various chemical reactions, including polymerization, oxidation, reduction, hydrolysis, and acid–base reactions. The strength of ReaxFF lies in its ability to describe complex intermolecular interactions during the reaction process, including bond length/angle changes and charge transfer. This allows it to accurately simulate complex chemical reaction processes.

ReaxFF simulations [25–27] in combination with a realistic macromolecular model of coal have emerged as a viable technique for investigating the relationship between chemical structural features and coal thermochemical reactivity at a molecular level [22,28–35]. In 2009, Salmon et al. [26,27] simulated the early coal formation process of Morwell lignite for the first time using the ReaxFF method, and examined the thermal decomposition processes of defunctionalization, depolymerization, and rearrangement of residual structures. Hong et al. [36] introduced calcium in the form of (-COO-Ca-OOC-) into a molecular model of coal and used ReaxFF MD simulations to investigate the effects of calcium on the pyrolysis process. Bang [37] investigated the effect of calcium on the co-pyrolysis of coal and polystyrene using ReaxFF; they found that calcium significantly promoted the co-pyrolysis process and the rapid cleavage of coal/polystyrene, resulting in a high yield of light tar. In conclusion, ReaxFF has important application value in coal pyrolysis, and it is crucial to choose a reasonable model to describe the reaction mechanism.

Based on these considerations, ReaxFF MD simulations were conducted to reproduce the transformation behavior of sodium at the atomic level. The ReaxFF MD simulation results were compared with flash pyrolysis–gas chromatography/mass spectrometry (Py-GC/MS) experimental data. The reaction pathways and the types of reaction were determined by monitoring the displacements of all intermediate species by the Chemical Trajectory Analyzer (ChemTraYzer2, CTY2) tool. Special attention was paid to the different forms of Na ($Na_{(g)}$, $NaOH_{(g)}$, tar-bonded sodium, and organic gas-bonded sodium) to obtain further details on the sodium migration in the pyrolysis process.

2. Experiments

2.1. Reactive force field (ReaxFF) simulation details

In our recent work, a molecular model of Zhundong coal containing organic sodium (as shown in Fig. 1) was constructed by combing ^{23}Na and ^{13}C nuclear magnetic resonance (NMR), Fourier transform infrared spectroscopy (FTIR), and sequential extraction experimental data [38].

The pyrolysis system consisted of 20 organic sodium-absorbed Zhundong coal molecules [$(C_{204}H_{157}N_3O_{38}SNa)_{20}$] in a 60 Å × 60 Å × 60 Å periodic cubic box, as shown in Fig. 2. The initial density of the system was set to 0.1 g/cm^3 to avoid atomic overlaps. The optimization process of the entire system was as follows: (1) annealing cycles ranging from 5 to 1000 K were carried out in the NVT ensemble, which maintains a constant number of particles (*N*), volume (*V*), and temperature (*T*) throughout the simulation. This approach allows the system to achieve equilibrium at a specified temperature. Energy minimization was carried out at each time step using the conjugate gradient algorithm; (2) compression and decompression were conducted in the NPT ensemble (constant number of particles, pressure (*P*), and temperature). This enabled the system to reach equilibrium under particular temperature and pressure conditions (0.02 GPa and 0.1 MPa, respectively); (3) geometry optimization was carried out in the NVE (microcanonical) ensemble, which maintains the number of particles, volume, and energy (*E*) constant without allowing energy or volume exchanges with the surroundings. This enables the analysis of the fundamental properties of the system while ensuring energy conservation.

With periodic boundary conditions for all simulations, the equations of motion were numerically integrated using the Verlet algorithm with a time step of 0.25 fs. The Berendsen thermostat [39] was used to control the system temperature, with a damping constant set to 100 fs. The Amsterdam Modeling Suite (AMS) software [40] was used to perform MD calculations of the optimized system at temperatures ranging from 2000 to 3200 K; the simulations were performed in the NVT ensemble for 200 ps, with a time step of 0.1 fs. The reaction force field file reported by Hou [41] was used in the calculations (see appendix for details).

As for the post-processing, the reaction pathway and type were determined using ChemTraYzer2, which is a tool for analyzing chemical reactions based on changes in bond orders [42,43]. The tool provides insights into the reaction mechanisms by visualizing the movements and interactions of atoms and molecules involved in the reaction. The output of the CTY2 tool is a visual representation of the reaction pathway, which can help researchers to understand complex reaction mechanisms and predict the products of chemical reactions. The critical level cutoff value, used for detecting and analyzing fragmentation and chemical events, was set to 0.3. Based on the CTY2 analysis, the reactions that involved different forms of Na were traced and statistically classified to provide further details on the sodium migration in the pyrolysis process. All data were averaged over five independent ReaxFF simulations.

Previous [33,44–46] ReaxFF simulations of thermochemical conversion processes, such as pyrolysis, gasification, and combustion of coal or char, typically adopted a strategy based on increasing the temperature. For example, a higher temperature ($T > 2000$ K) was selected for the simulation for two reasons [33,44–46]. The timescale of MD simulations, in the picosecond to nanosecond range, is substantially shorter than that of actual macroscopic observations (ranging from milliseconds to seconds), so the selected temperature of the ReaxFF simulations was much higher than the experimental temperature, which accelerated the atomic motions in the system and improved the simulation efficiency [47].

2.2. Pyrolysis–gas chromatography/mass spectrometry (Py-GC/MS) experiments

The pyrolysis of Zhundong coal was carried out using a Py-GC/MS analyzer (Agilent 7890A-5975 C, USA). A coal sample was heated to

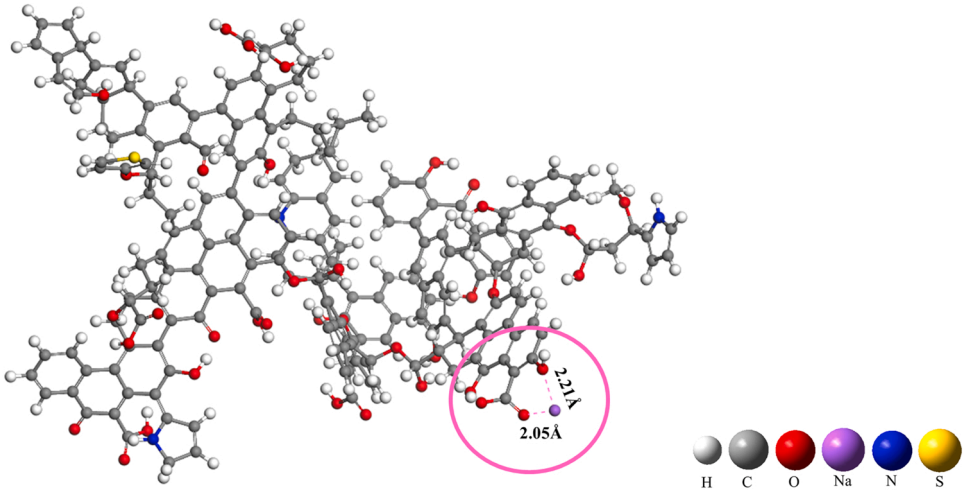

Fig. 1. Model of organic sodium-absorbed Zhundong coal, $C_{204}H_{156}N_3O_{38}SNa$ [38].

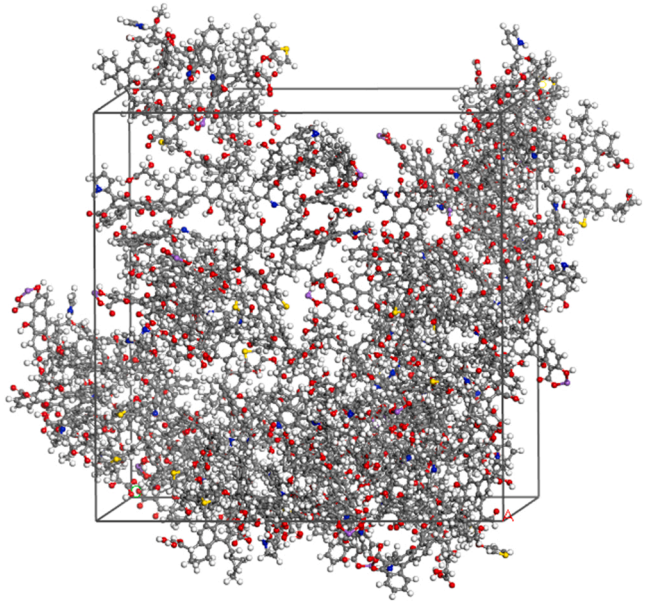

Fig. 2. Snapshot of initial configuration of Zhundong coal pyrolysis system.

600 ℃ at a rate of 1.8×10^4 ℃/s under a high-purity protective atmosphere, and a TR-5MS capillary column (30 m, 0.25 mm, i.e., 0.25 μm film thickness) was used for separation. At an electron impact ionization energy of 70 eV, the transfer line temperatures were set to 250 ℃. High-purity helium (≥ 99.999%) was used as a carrier gas at a flow rate of 1 mL/min. Injections were performed in splitless mode. The GC oven temperature started at 40 ℃ and was held constant for 3 min. Then, it was increased to 220 ℃ at a rate of 5 °C/min and maintained for 5 min

3. Results and discussion

3.1. Simulation validation

Pyrolysis products originating from the direct cleavage of the structure of Zhundong coal were detected by the Py-GC/MS technique. To validate the simulations, the ReaxFF MD results were compared with the experimental data. The major products observed in the Py-GC/MS experiments were light tar components. Therefore, the light tar components observed in the ReaxFF MD simulations were compared with the experimental results. As shown in Table 2, the primary pyrolysis products identified in the Py-GC/MS pyrolysis experiments, as well as the products and intermediates observed at 3000 K in the ReaxFF simulations of the Zhundong coal pyrolysis process (Table 3), included benzene, acenaphthene, fluorene, and naphthalene. In general, the compounds detected by Py-GCMS were also observed in the ReaxFF simulations. In addition, the ReaxFF simulations detected some important intermediate products (such as C_7H_4, C_7H_6, $C_{11}H_6$, $C_{11}H_8$, $C_{12}H_{10}$, $C_{12}H_9$, and $C_{12}H_7O$). There were some differences between experiments and simulations, whose results could not be fully matched. As a result, when comparing experimental and simulation results, it is necessary to carefully assess whether each compound has been observed in the simulation. Although some compounds, including C_7H_8, $C_{11}H_{10}$, $C_{12}H_8$, $C_{12}H_8S$, and $C_{12}H_8O$ (detected in Py-GCMS experiments) were not observed in the ReaxFF simulations, the corresponding unsaturated precursors, such as C_7H_4, C_7H_6, $C_{11}H_6$, $C_{11}H_8$, $C_{12}H_{10}$, $C_{12}H_9$, and $C_{12}H_7O$, were detected in the simulation data. This indicates that the ReaxFF simulations provide a relatively accurate description of the actual system and can therefore be used for predicting and studying the

Table 2
Molecule of light tar presented in Py-GC/MS experiment and ReaxFF simulation.

Formula	Simulation	Py-GC/MS
$C_5H_4O_2$	Yes	—
C_5H_5	Yes	—
C_6H_6	Yes	Yes
C_6H_6O	Yes	—
C_6H_7NO	Yes	—
C_7H_6	Yes	—
C_7H_8	—	Yes
C_8H_4S	Yes	—
C_8H_6	Yes	—
$C_8H_6O_2$	Yes	—
C_8H_7N	Yes	—
C_8H_8	Yes	Yes
C_8H_8O	Yes	—
$C_9H_6O_2$	Yes	—
C_9H_8	Yes	Yes
$C_{10}H_6$	Yes	—
$C_{10}H_8$	Yes	Yes
$C_{11}H_8$	Yes	—
$C_{11}H_{10}$	—	Yes
$C_{12}H_8$	—	Yes
$C_{12}H_{10}$	Yes	Yes
$C_{12}H_8S$	—	Yes
$C_{12}H_8O$	—	Yes
$C_{13}H_{10}$	Yes	Yes

Note: —, No discovery

Table 3
Distribution of ReaxFF pyrolysis products and intermediates at 3000 K.

Inorganic No	Gases molecule	C_{1-4} No	Compounds molecule	C_{5-13} No	Compounds molecule	C_{14-39} No	Compounds molecule	C_{40+} No	Compounds molecule
417	CO	6	CH_2N	4	C_5H_3	1	$C_{14}H_6$	1	$C_{40}H_{16}$
24	CO_2	33	CH_2O	2	C_5H_3N	1	$C_{14}H_7O$	1	$C_{41}H_{21}N$
2	H	1	CH_2O_2	1	C_5H_3O	1	$C_{14}H_8N$	1	$C_{42}H_{19}O_3S$
249	H_2	1	CH_2OS	4	C_5H_4	1	$C_{14}H_8O$	1	$C_{42}H_{22}$
76	H_2O	4	CH_3	1	C_5H_4N	1	$C_{15}H_{11}$	1	$C_{43}H_{25}$
11	H_2S	3	CH_3N	1	C_5H_4O	1	$C_{15}H_8$	1	$C_{44}H_{20}N_2O_2$
1	H_3N	1	CH_3NaO	1	$C_5H_4O_2$	1	$C_{17}H_{11}O_2$	1	$C_{45}H_{27}O_2$
4	HNaO	3	CH_4	2	C_5H_5	1	$C_{17}H_5O$	1	$C_{47}H_{25}O$
1	HO	7	CHN	1	C_6H_2O	1	$C_{18}H_{11}$	1	$C_{50}H_{28}O_2$
14	Na	2	CHNO	1	C_6H_3	1	$C_{18}H_9$	1	$C_{53}H_{27}NO_3$
		44	CHO	1	C_6H_4	1	$C_{19}H_{13}O_2$	1	$C_{62}H_{35}O$
		3	C_2H	1	C_6H_4N	1	$C_{20}H_{12}$	1	$C_{63}H_{34}NO_4$
		164	C_2H_2	1	C_6H_4O	1	$C_{20}H_{13}$	1	$C_{64}H_{34}$
		1	C_2H_2N	2	C_6H_5	1	$C_{20}H_9O_2$	1	$C_{69}H_{25}O_4$
		1	C_2H_2NaO	1	C_6H_5O	1	$C_{21}H_9O_2$	1	$C_{69}H_{36}NO_2$
		7	C_2H_2O	5	C_6H_6	1	$C_{22}H_{14}O_2$	1	$C_{75}H_{40}N$
		2	C_2H_2S	1	C_6H_6O	1	$C_{23}H_{10}$	1	$C_{81}H_{40}NO_3$
		55	C_2H_3	1	C_6H_7NO	1	$C_{23}H_{11}O$	1	$C_{96}H_{50}N$
		6	C_2H_3N	1	C_7H_4	1	$C_{23}H_{13}O$	1	$C_{129}H_{66}NO_2$
		2	C_2H_3O	1	C_7H_5O	1	$C_{23}H_{14}S$	1	$C_{174}H_{75}NO_3$
		6	C_2H_4	1	C_7H_6	1	$C_{24}H_{12}O_2$	1	$C_{192}H_{86}NO_4$
		1	C_2H_5N	1	C_8H_4S	1	$C_{24}H_8$	1	$C_{217}H_{100}N_3O_8$
		11	C_2HO	1	C_8H_5	1	$C_{26}H_{13}N_2$		
		1	C_2HS	1	C_8H_6	1	$C_{26}H_{16}$		
		3	C_3H	1	$C_8H_6O_2$	1	$C_{28}H_{14}$		
		3	C_3H_2	2	C_8H_7	1	$C_{29}H_{18}$		
		3	C_3H_2O	1	C_8H_7N				
		17	C_3H_3	1	C_8H_7O				
		1	C_3H_3N	2	C_8H_8				
		2	C_3H_3NO	1	C_8H_8O				
		2	C_3H_3O	1	C_9H_6				
		6	C_3H_4	1	$C_9H_6O_2$				
		1	C_3H_4N	1	C_9H_7O				
		1	C_3H_5	2	C_9H_8				
		2	C_3HO	1	$C_{10}H_4O$				
		1	C_3NO	1	$C_{10}H_4OS$				
		1	C_4H	1	$C_{10}H_6$				
		8	C_4H_2	2	$C_{10}H_7$				
		1	C_4H_2N	1	$C_{10}H_8$				
		1	C_4H_2O	1	$C_{11}H_5O_3$				
		11	C_4H_3	1	$C_{11}H_6$				
		1	C_4H_3N	1	$C_{11}H_6O$				
		1	C_4H_3S	1	$C_{11}H_8$				
		4	C_4H_4	1	$C_{11}H_9O$				
		1	C_4H_4N	1	$C_{12}H_{10}$				
		1	C_4H_5	2	$C_{12}H_7O$				
				1	$C_{12}H_9$				
				2	$C_{13}H_{10}$				
				1	$C_{13}H_{10}N$				
				1	$C_{13}H_7$				

interactions between the relevant compounds.

It should be noted that the primary application of py-GCMS is the detection of volatile and semivolatile organic compounds. In our study, we employed py-GCMS to analyze the volatile constituents of Zhundong coal and confirm the accuracy of the ReaxFF simulations. Nevertheless, this technique exhibits intrinsic limitations in the detection of sodium compounds, owing to their low relative abundance among the volatile components. Furthermore, the high polarity and molecular weight of organic sodium compounds may lead to inadequate separation, ultimately impacting the precise detection of these species. These constraints should be carefully considered when interpreting the results of our py-GCMS analysis.

Future research could focus on employing complementary techniques or improving existing methodologies to accurately detect and quantity these species in the context of coal pyrolysis.

3.2. Migration and transformation of sodium

3.2.1. Direct observation of molecular dynamics trajectories

To elucidate the reaction pathway of sodium, we initially conducted a direct observation of atomic trajectories generated by the ReaxFF simulations, which provided preliminary insights into the mechanism responsible for the conversion of solid-phase organic sodium into its gaseous counterpart.

Fig. 3 shows a snapshot of the molecular pyrolysis process of Zhundong coal, in which sodium reacted with the coal matrix. Based on the snapshot, the $Na_{(g)}$ migrated toward the coal molecule via thermal motion (Fig. 3a) and subsequently became trapped within the reticular pores of the coal molecule (Fig. 3b-c). Following this, the $Na_{(g)}$ established ternary coordination with oxygen atoms in the coal molecule (Fig. 3e-f). Once the $Na_{(g)}$ formed multiple coordination bonds with the coal oxygen atoms, those with weaker chemical bonds were initially captured by sodium, resulting in the formation of an -O-Na-OH structure (Fig. 3g), followed by NaOH formation (Fig. 3h). This chemical reaction process can be represented as follows (reaction 1):

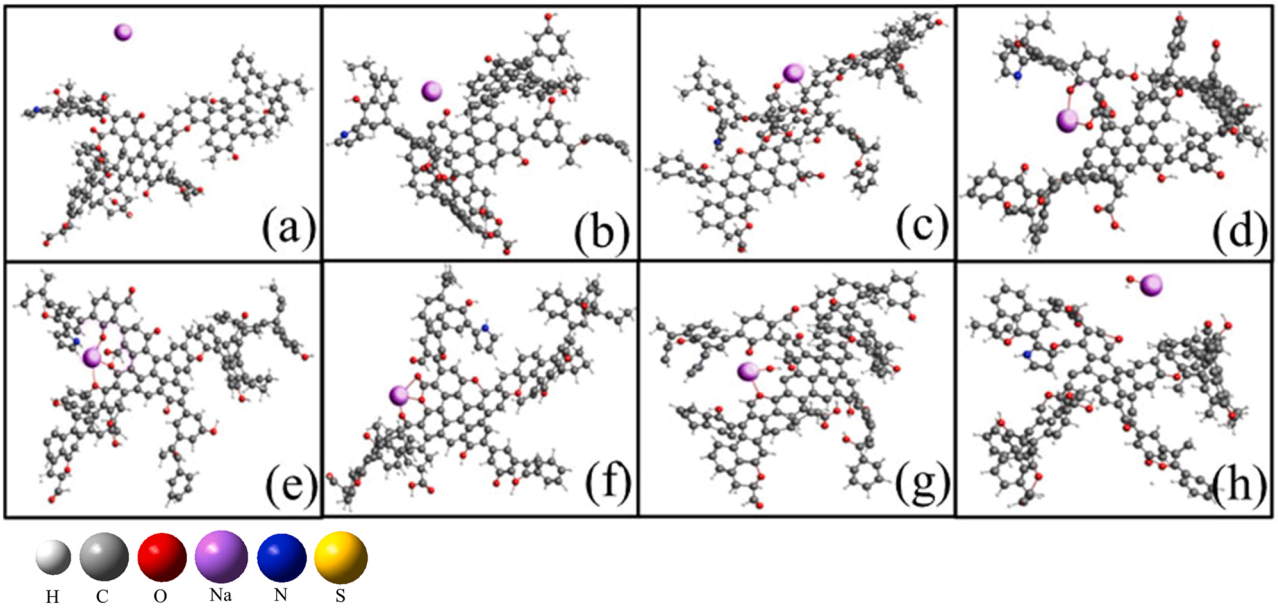

Fig. 3. Snapshots of the pyrolysis process of Zhundong coal observed during the ReaxFF simulation, showing a sodium atom reacting with the coal matrix.

Fig. 4 shows snapshots of the pyrolysis reaction of the Zhundong coal molecule, in which organic sodium reacted with OH radicals. According to the snapshots of the ReaxFF reaction, OH radicals were first captured by organic sodium after its thermal movement to the vicinity on the coal molecule (Fig. 4a–c), resulting in the formation of Na–O coordination bonds. Then, they underwent a series of deformations and migrations to form R-C- and NaOH structures (Fig. 4d–h). This process could be represented as follows (reaction 2):

$$\text{R-C-ONa} + \text{OH} \rightarrow \text{R-C=O} + \text{NaOH} \quad (2)$$

As shown in Fig. 4, sodium served as a crosslinking point during pyrolysis and frequently coordinated oxygen and carbon atoms of the coal matrix. This promoted the twisting motion of coal molecules and strengthened their three-dimensional (3D) network. The presence of $Na_{(g)}$ inhibited the formation of polycyclic aromatic hydrocarbon molecules into char with a graphene-like structure.

Fig. 5 shows ReaxFF simulation snapshots of the pyrolysis reaction of the Zhundong coal molecule, in which $Na_{(g)}$ reacted with the coal matrix to form hydrated sodium ions. These snapshots reveal that the $Na_{(g)}$ underwent thermal motion near the coal molecule and were initially captured by its carboxyl oxygen (Figs. 5a and 5b), forming a -COOH-Na structure. Under the coordination influence of sodium, electron transfer occurred between sodium and oxygen atoms, which weakened the carbon–oxygen bond in the carboxyl group. Subsequently, the $Na_{(g)}$ captured the hydroxyl group from the carboxyl group, leading to the formation of the NaOH intermediate. After the OH was captured by the $Na_{(g)}$, the C=O structure in the original carboxyl group became unstable, resulting in the generation of CO (Fig. 5c–e), as shown in reaction 3. The newly formed NaOH then captured another hydrogen atom from the methyl group, resulting in the formation of a stable $Na{\cdot}H_2O$ species (Fig. 5f–j), as summarized in reaction 4:

$$\text{Na} + \text{R-COOH} \rightarrow \text{R'} + \text{NaOH} + \text{CO} \quad (3)$$

$$\text{R'}+\text{NaOH}\rightarrow\text{R''}+\text{Na}{\cdot}\text{H}_2\text{O} \quad (4)$$

Fig. 6 shows ReaxFF simulation snapshots of the pyrolysis of Zhundong coal, in which the cleavage of organic sodium produced NaOH (reaction 5). Initially, sodium formed a binary coordination structure with the carboxyl and carbonyl oxygens. As the pyrolysis reaction progressed, the coordination bond between the $Na_{(g)}$ and the carbonyl oxygen was cleaved (Figs. 6a and 6b). Subsequently, the oxygen linked to the $Na_{(g)}$ on the carboxyl group was also cleaved, leading to the formation of NaOH under the $Na_{(g)}$'s adsorption (Fig. 6c–f).

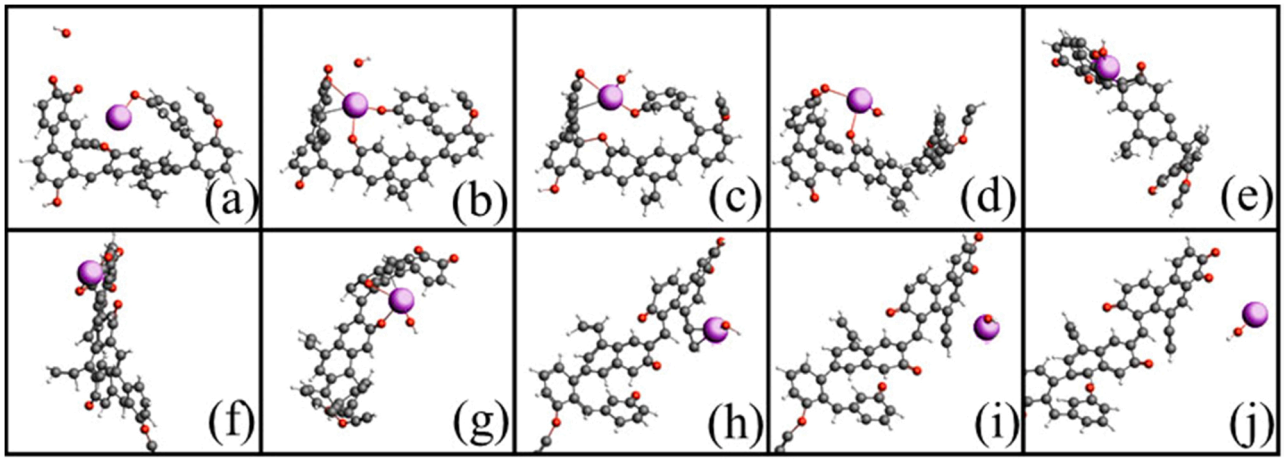

Fig. 4. Snapshots of the pyrolysis process of Zhundong coal observed during the ReaxFF simulation, showing an organic sodium atom reacting with OH radicals.

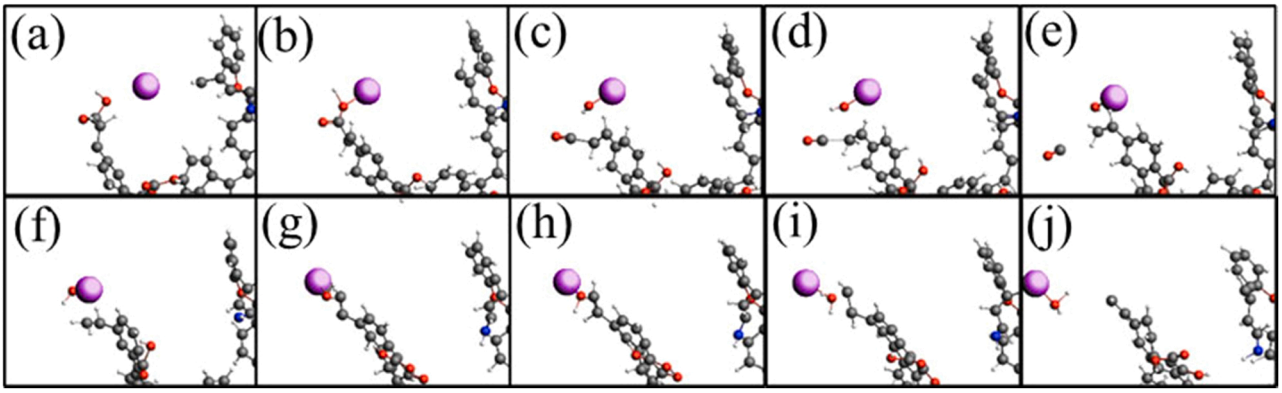

Fig. 5. Snapshots of the pyrolysis process of Zhundong coal observed during the ReaxFF simulation, showing the reaction of a sodium atom with coal molecules to form CO and hydrated sodium species.

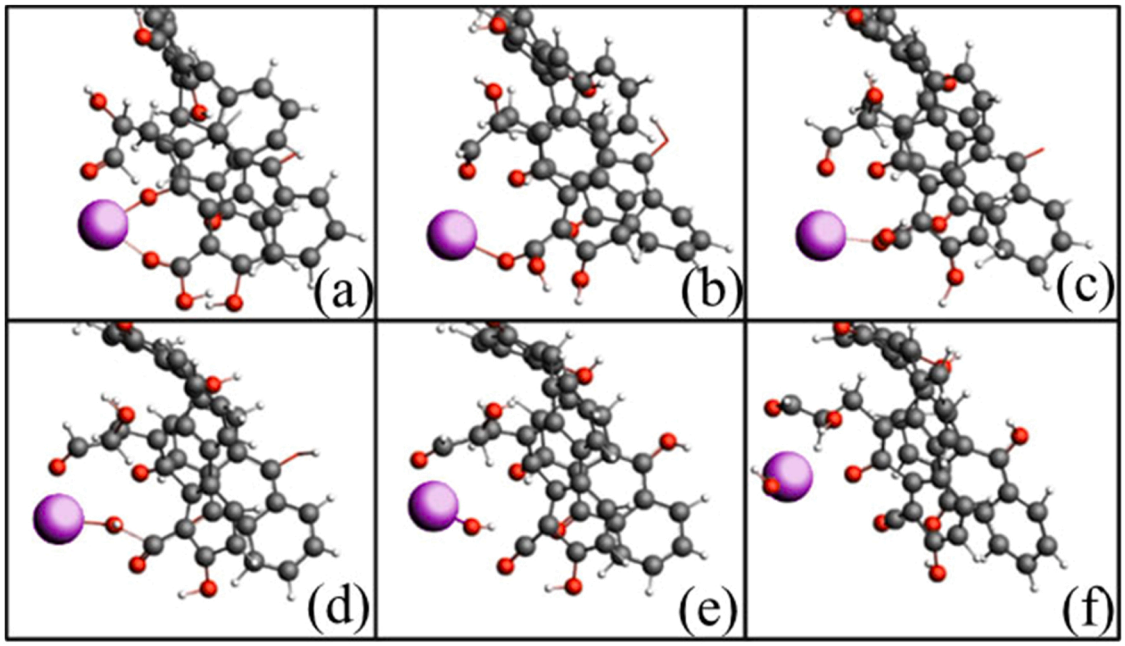

Fig. 6. Snapshots of the pyrolysis process of Zhundong coal observed during the ReaxFF simulation, showing the cleavage of organic sodium to form NaOH.

$$\text{R-ONa} \rightarrow \text{R'} + \text{NaOH} \quad (5)$$

Fig. 7 shows three snapshots of NaOH (formed from organic sodium) participating in the pyrolysis reaction. Fig. 7(A) shows that NaOH attacked the macromolecular coal fragment to produce a $Na_{(g)}$ and a H_2O molecule after capturing a hydrogen atom of the six-membered ring. Fig. 7(B) shows the attack of NaOH to the hydroxyl group of the coal macromolecule, to form a hydrated sodium ion after obtaining a hydrogen atom from the hydroxyl group. In contrast, the hydroxyl group of the coal fragment was converted to an aldehyde group. Fig. 7(C) shows the catalytic reaction of NaOH with CHO_2 and the cleavage product of coal molecules, in which CHO_2 was cleaved, generating a hydrogen atom and a carbon dioxide molecule in the presence of NaOH.

In summary, the inherent organic sodium in the coal molecule with 3D network structure was unstable, and could form binary or multiple coordination structures with oxygen atoms of the coal matrix during the pyrolysis process; the first step for sodium removal was the conversion of organic-bonded sodium to Na, NaOH, or $Na{\cdot}H_2O$.

3.2.2. *Na-containing gases*

In addition to the direct observation of the atomic trajectory, we also determined the number of sodium-containing products that were generated and the number of chemical reactions that occurred during the pyrolysis process, in order to further clarify the statistical mechanics of the conversion of solid-phase organic sodium to its gas-phase counterpart.

Fig. 8 shows the distributions of typical inorganic Na-containing gases obtained from the ReaxFF simulation. As discussed in Section 3.2.1, the bonds between sodium and the carbon matrix are constantly formed and broken during the coal pyrolysis process; thus, the curve in Fig. 8 displays slight fluctuations. The main components of the inorganic Na-containing gases were Na atoms, followed by NaOH and $Na{\cdot}H_2O$. This is consistent with the reported experimental results on the online detection of K, KOH, and KCl [48,49] in an anoxic environment (fuel-rich methane–air flat flames), which showed that K atoms account for the most significant proportion of gaseous potassium released from biomass combustion, followed by KOH.

As the temperature increased, the proportion of $Na_{(g)}$ in the sodium-containing gas-phase products gradually increased, because more sodium-containing species underwent cleavage and formed $Na_{(g)}$ at

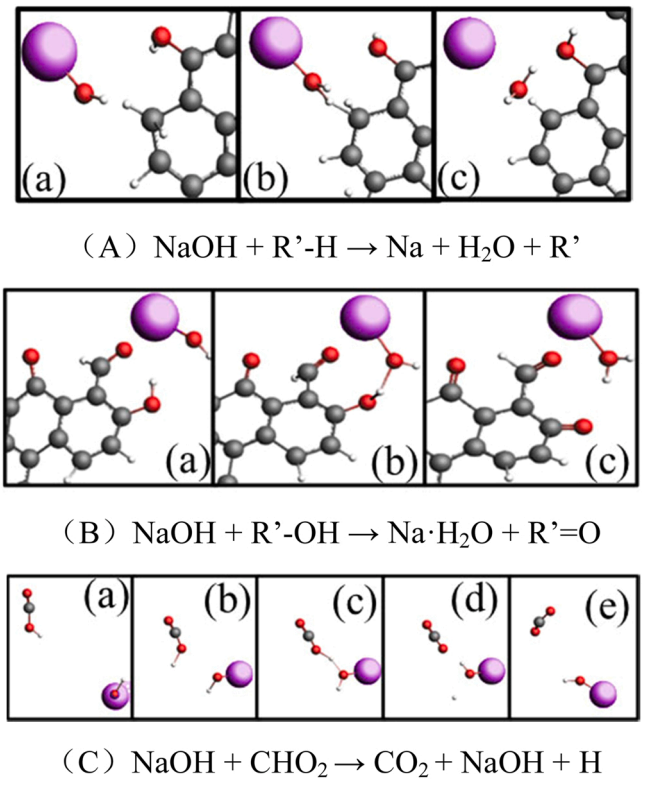

Fig. 7. Snapshots of the pyrolysis process of Zhundong coal observed by ReaxFF simulation: the produced NaOH continues to participate in the pyrolysis reaction.

higher temperatures. In addition, the NaOH proportion showed an initial increase followed by a decrease. This may be because NaOH was released in the early stage of pyrolysis and then involved in the subsequent reaction of the pyrolysis process, resulting in its consumption.

Fig. 9 shows the distributions of the other three forms of sodium observed in the ReaxFF simulations at different temperatures: $C_{40+}Na$ (char sodium), $C_{5-39}Na$ (tar sodium), $C_{1-4}Na$ (volatile sodium). As shown in Fig. 9a, the amount of $C_{1-4}Na$ increased with increasing temperature and time. This increase is attributed to the breaking down of large organic sodium molecules into smaller molecular sodium compounds with increasing pyrolysis temperature and time. The trend observed in Fig. 9b, showing the concentration of C_{5-39} Na initially rising and subsequently declining with increasing temperature and time, may be attributed to the participation of $C_{5-39}Na$ in further chemical reactions, which contribute to the formation of other sodium species, such as inorganic sodium compounds or atomic sodium. As shown in Fig. 9c, the concentration of $C_{40+}Na$ gradually decreased over time, and its content further decreased with increasing temperature. The initial organic sodium species present in coal was $C_{40+}Na$, as shown in Fig. 1. As the reaction progressed, $C_{40+}Na$ was gradually broken down into small molecules, and the cleavage reaction rate intensified with increasing temperature, both of which led to a reduction in the $C_{40+}Na$ content. Combined with the direct observation of the atomic trajectories in Section 3.2.1, it is clear that the migration process of sodium during thermostatic pyrolysis can be divided into two steps. First, organic sodium undergoes thermal degradation to generate small $Na_{(g)}$ or NaOH. Then, the generated $Na_{(g)}$ and $NaOH_{(g)}$ react with coal molecules, leading to their further decomposition. The reaction process can be expressed as follows:

$$R\text{-}O\text{-}Na \rightarrow R' + Na_{(g)} \quad (6)$$

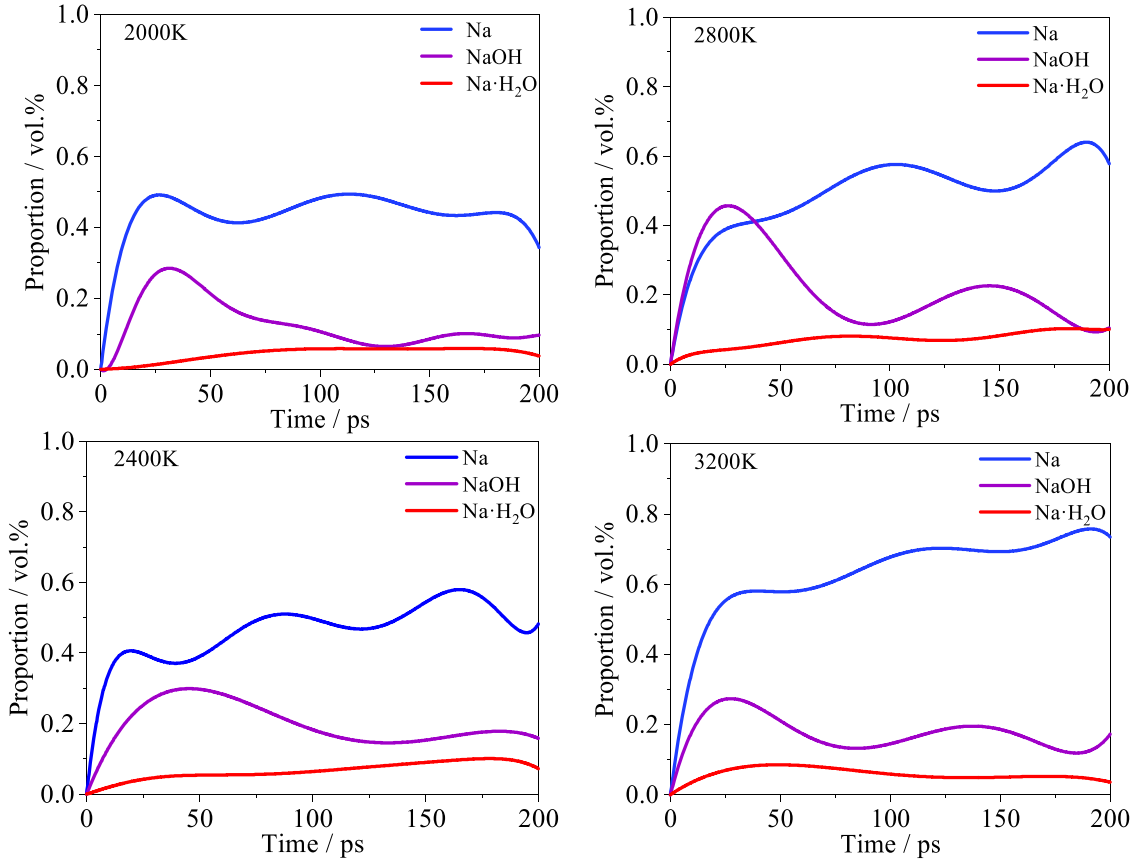

Fig. 8. Time evolution of inorganic sodium-containing gaseous products of Zhundong coal pyrolysis.

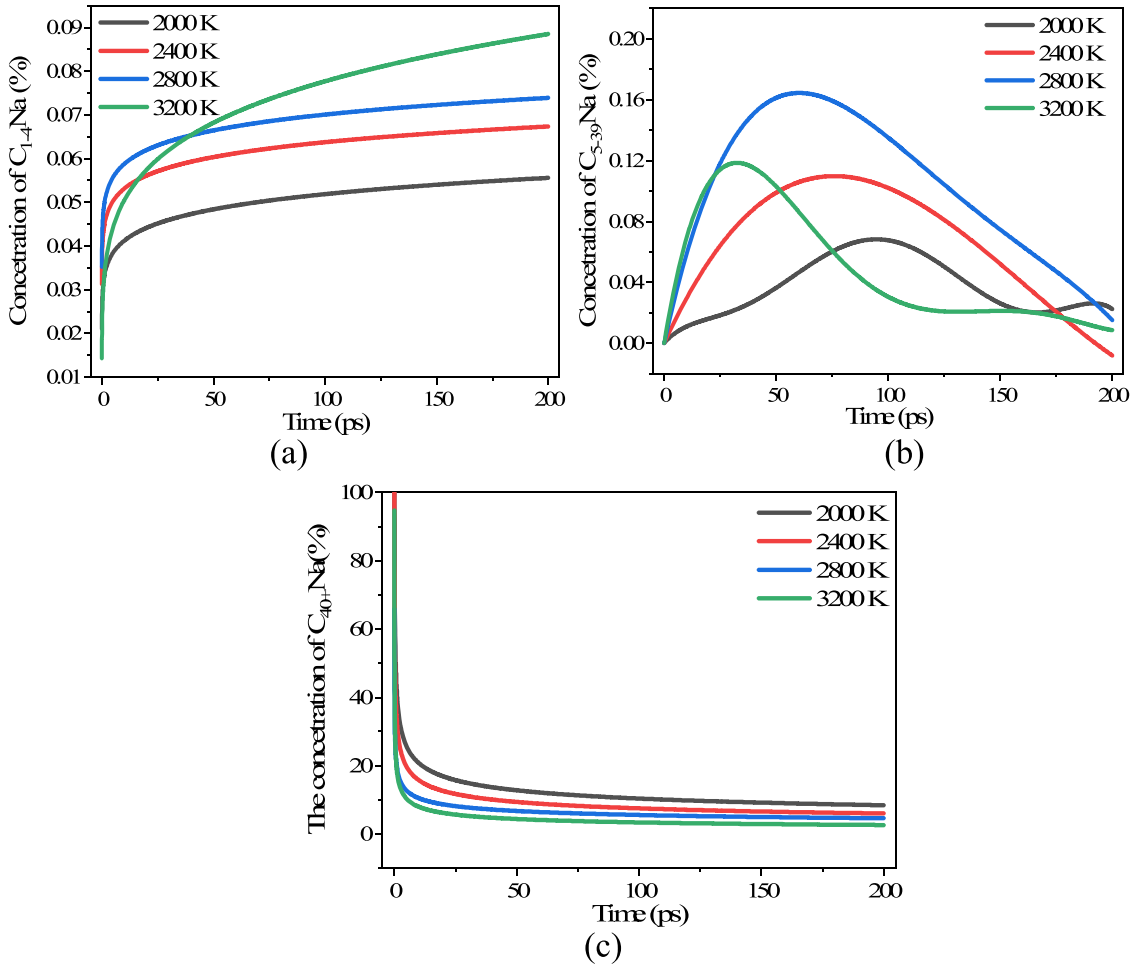

Fig. 9. Time evolution of $C_{40+}Na$ (char sodium), $C_{5-39}Na$ (tar sodium), $C_{1-4}Na$ (volatile sodium) concentrations during the ReaxFF simulation.

$$R' + Na_{(g)} \rightarrow R'\text{-O-Na} \rightarrow R'' + Na_{(g)} \text{ (or } NaOH_{(g)} \text{ or } Na{\cdot}H_2O) \quad (7)$$

3.3. Effect of sodium on the distribution of pyrolysis products

ReaxFF MD simulations of the pyrolysis processes of sodium-containing and sodium-free systems were performed to investigate the effect of sodium on the coal pyrolysis reactions from a microscopic perspective. The influence of sodium on the pyrolysis of Zhundong coal was evaluated by comparing the distributions of gas products in systems with and without sodium.

The products were classified as follows: those with 0–4 carbon atoms (C_{0-4}) were characterized as gaseous, whereas those with 5–39 carbon atoms (C_{5-39}) were classified as tar; molecules with more than 40 carbon atoms (C_{40+}) were referred to as char.

Fig. 10 shows the temporal evolution of the gas, tar, and char fractions during the simulation of the Zhundong coal pyrolysis. In a comparative analysis of the time evolution of char at various temperatures, both in the presence and absence of organic sodium, it was observed that organic sodium facilitated the decomposition of char within the temperature range of 1800–2400 K. Conversely, between 2600 K and 3200 K, organic sodium appeared to inhibit the breakdown of char. At simulation temperatures of 1800 and 3200 K, organic sodium exhibited an inhibitory effect on gas formation. At 1800–2400 K, the presence of organic sodium promoted the amount of tar produced by pyrolysis; however, at 2600–3200 K, it reduced the amount of tar. Deng et al. and Sathe et al. [50] also found that organic sodium promoted the precipitation of volatile fractions during low-temperature pyrolysis. In contrast, at high temperatures (> 500 ℃), organic sodium inhibited the pyrolysis process of coal, similar to the findings of this work. Combined with the direct observation of MD trajectories in Section 3.2.1, these results show that a network structure with sodium serving as crosslink point is formed as the pyrolysis proceeds. This, in turn, enhanced the interconnection between macromolecular species, hindering the release of small molecular fragments of tar and other species from the network.

3.4. Reaction pathways of sodium

The total number of sodium production reactions was then identified by tracking their corresponding amounts. As shown in Fig. 11, the total number of reactions increased with the temperature, indicating that a high temperature could accelerate the reaction process. During the pyrolysis, most of the organic sodium species, such as $C_{40+}Na$ (char sodium), $C_{5-39}Na$ (tar sodium), and $C_{1-4}Na$ (volatile sodium), were converted to $Na_{(g)}$, with only a small proportion being directly released as NaOH and $Na{\cdot}H_2O$.

The majority of $Na_{(g)}$ were found to originate from organic sodium ($C_{1-40+}Na$), with a minor contribution from NaOH and $Na{\cdot}H_2O$. The generation of NaOH and $Na{\cdot}H_2O$ was primarily due to the presence of $Na_{(g)}$, with only a limited number originating from organic sodium ($C_{1-40+}Na$). The interconversion between NaOH and $Na{\cdot}H_2O$ primarily took place through $Na_{(g)}$ serving as intermediates, whereas only a limited number of direct conversion reactions between NaOH and $Na{\cdot}H_2O$ was observed (see Tables A1 and A2 in the Appendix for details).

To examine the migration and transformation of sodium in detail, the main reaction network between Na-containing species was determined using the CTY2 tool. As shown in Fig. 12, there was no direct conversion

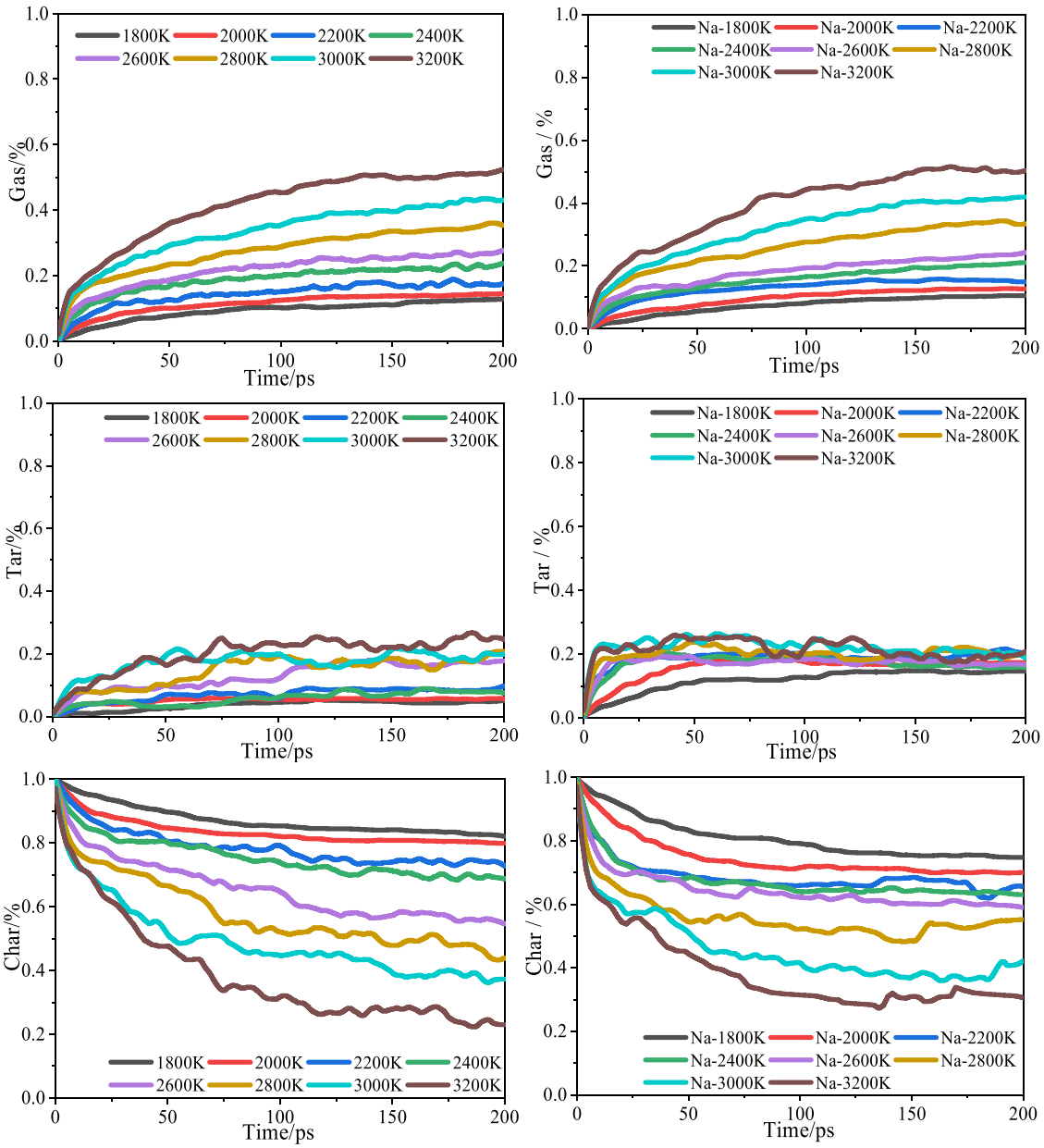

Fig. 10. Time evolution of gas, tar, and char fractions during thermostatic pyrolysis at different temperatures.

relationship between $C_{40+}Na$ and $C_{5-39}Na$ or $C_{1-4}Na$. $C_{40+}Na$ was initially decomposed into $Na_{(g)}$ or $NaOH_{(g)}$. sodium atoms, or NaOH then continued to reacted with tar (C_{5-39}) to form organic sodium with a low carbon number.

The generation of $Na_{(g)}$ from different types of organic sodium ($C_{1-40+}Na$) was found to involve different reaction pathways. More specifically, $C_{40+}Na$ underwent direct cleavage or reacted with -H, hydrocarbon radicals, oxygen-containing intermediates, H_2O, and CO to generate $Na_{(g)}$. $C_{5-39}Na$ underwent direct cleavage or reacted with -H to generate $Na_{(g)}$. At the same time, $C_{1-4}Na$ underwent direct cleavage or reacted with H_2O, CO, and CO_2 to produce $Na_{(g)}$. Additionally, $C_{40+}Na$, $C_{5-39}Na$, and $C_{1-4}Na$ were observed to undergo direct cleavage and yield NaOH, and $C_{40+}Na$ was also observed to react with -OH to produce NaOH. NaOH, $Na_{(g)}$, and Na-H_2O could interconvert into one another. The most diverse reaction pathways were observed between NaOH and $Na_{(g)}$, and included the direct decomposition (DP) of NaOH or its reaction with·H, hydrocarbon radicals, oxygen-containing intermediates, H_2O, or CO to generate $Na_{(g)}$. The $Na_{(g)}$ could also combine with OH, hydrocarbons, oxygen-containing intermediates, or organic compounds to form NaOH. On the other hand, a few types of reactions could take place between NaOH and Na·H_2O, including the reaction of NaOH with organic compounds, H_2O, hydrocarbons, OH, and·H to generate Na·H_2O, as well as the DP or reaction of Na·H_2O with·OH and organic compounds to form NaOH. The reactions between Na and Na·H_2O were the least numerous, including the reaction of $Na_{(g)}$ with hydrocarbons and H_2O to form Na·H_2O and the DP or reaction of Na·H_2O with hydrocarbons to produce $Na_{(g)}$.

Compared to traditional experimental methods, the ReaxFF MD simulations detected more radical reactions, such as those of hydrocarbon groups [·R (·C_2H/·CH_3/·C_3H_2/·C_2H_3),·H,·OH], and some small-molecule intermediates (CH_3O, C_2H_3O) were involved in the reaction. It was also clear from the proposed mechanism that Na was the main conversion center, and more types of reactions produced sodium. The detailed reactions identified with the CTY2 tool are provided in the Supplementary Material.

In light of the challenges associated with quantitative analysis in coal

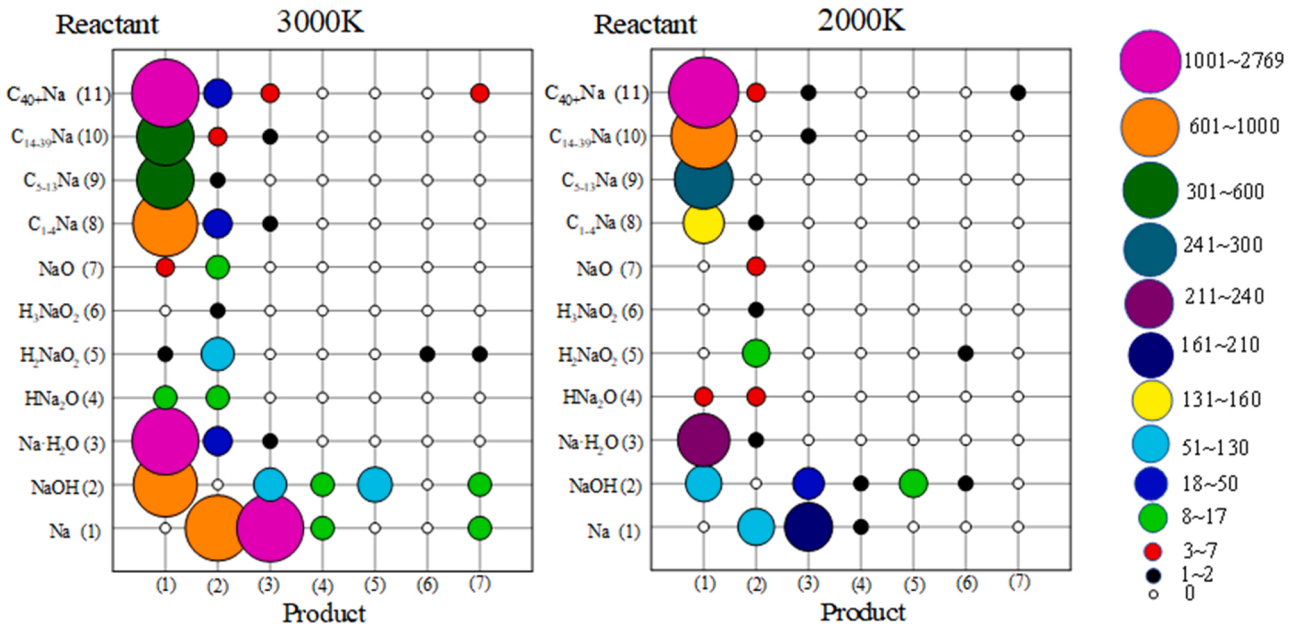

Fig. 11. Reaction matrix of existing forms of sodium.

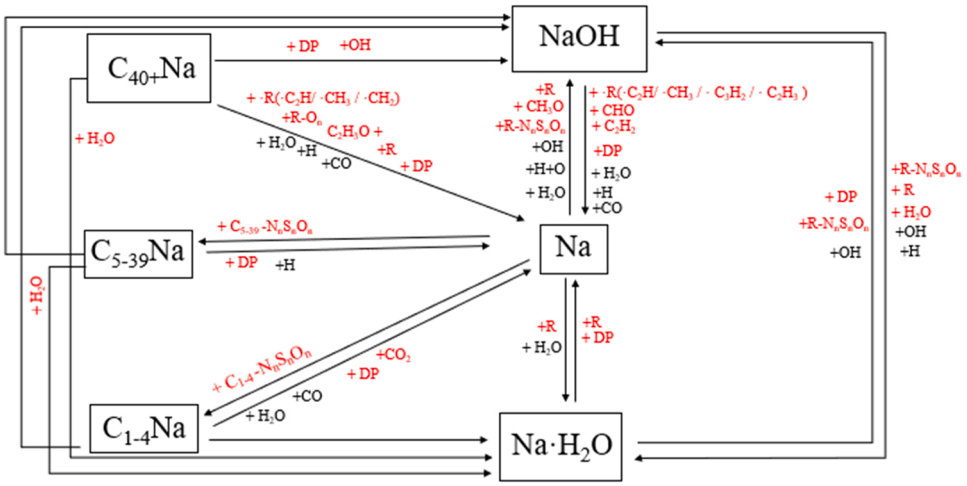

Fig. 12. Reaction network for the migration and transformation pathways of sodium (red: unique pathways found in this work), where DP refers to Direct Decomposition.

pyrolysis, future research should aim to develop more robust and reliable quantitative methods for characterizing the complex products formed during this process. Advancements in analytical techniques, such as multidimensional chromatography, might enhance the separation and identification of these compounds. Additionally, the integration of computational and experimental approaches, including advanced molecular simulations, may provide a more comprehensive understanding of the underlying pyrolysis mechanisms and the effects of various parameters on product formation.

4. Conclusion

In this work, the mechanism of migration and transformation of inherent organic sodium during the pyrolysis process of Zhundong coal was examined at the molecular level through ReaxFF simulations. The different forms of sodium ($Na_{(g)}$, $NaOH_{(g)}$, tar-bonded sodium, and organic gas-bonded sodium) were carefully analyzed to gain insights into their migration during the pyrolysis process.

The simulation results were compared to experimental Py-GC/MS data, and a good agreement was found between the observed representative products such as benzene, naphthalene, fluorene, and acenaphthene.

Inherent organic sodium was unstable in the coal molecule with 3D network structure, and mainly coordinated multiple oxygen atoms rather than carbon atoms. During pyrolysis, inherent organic sodium was transformed into three main sodium species: Na atoms, NaOH, and $Na{\cdot}H_2O$. These sodium atoms, NaOH and $Na{\cdot}H_2O$, constantly interacted with the coal molecular matrix throughout the subsequent pyrolysis process to produce sodium complexes, which facilitated the accumulation of polycyclic aromatic hydrocarbons. These sodium-containing intermediates repeatedly reacted with the coal matrix, which strengthened its three-dimensional network and thus reduced the degree of graphitization of the char produced by the pyrolysis process.

$C_{40+}Na$ was mainly decomposed into $Na_{(g)}$ or NaOH, which then reacted with tar (C_{5-39}) or gas (C_{1-4}) to form tar-bonded sodium, or organic gas-bonded sodium, respectively. The tar-bonded sodium, or organic gas-bonded sodium was further continued to decomposed or combined with H_2O to form NaOH, $Na_{(g)}$, or $Na{\cdot}H_2O$. The majority of

$Na_{(g)}$ were found to originate from organic sodium ($C_{1-40+}Na$), with a minor contribution from NaOH and $Na{\cdot}H_2O$. The generation of NaOH and $Na{\cdot}H_2O$ was primarily due to the presence of $Na_{(g)}$, with only a limited number originating from organic sodium ($C_{1-40+}Na$). The results also show that organic sodium inhibits char and tar formation at high temperatures, whereas at low temperatures it promotes char formation and inhibits tar production.

Although the simulations do not allow a quantitative analysis of the results, they can be used for the qualitative analysis of the products and reaction pathways. Understanding the product profiles and generation processes provides helpful information for elucidating the migration and transformation of organic sodium in coal.

CRediT authorship contribution statement

Cen Sun (First Author):Conceptualization, Methodology, Software, Investigation, Formal Analysis, Writing - Original Draft;Writing - Review & Editing. **Aixue Zhu:** Data Curation, Writing - Original Draft, Visualization, Investigation; Writing-Review & Editing. **Tong Xu:** Review & Editing. **Xiaolin Wei** (Corresponding Author)**:** Funding Acquisition; Conceptualization. Dikun Hong**:** Validation. Tong Si**:** Visualization**:**Review & Editing.

Declaration of Competing Interest

The authors declare that they have no conflict of interest.

Data availability

Data will be made available on request.

Acknowledgements

The authors acknowledge the support of the National Science Foundation of China (No. 51736010). The authors would like to express their sincere gratitude to Professor Xiaoxia Li for her invaluable suggestions.

Appendix A. Supporting information

Supplementary data associated with this article can be found in the online version at doi:10.1016/j.jece.2023.110189.

References

[1] P. Glarborg, P. Marshall, Mechanism and modeling of the formation of gaseous alkali sulfates, Combust. Flame 141 (1–2) (2005) 22–39, https://doi.org/10.1016/j.combustflame.2004.08.014.
[2] H. Fatehi, Y. He, Z. Wang, Z.S. Li, X.S. Bai, M. Aldén, et al., Libs measurements and numerical studies of potassium release during biomass gasification, Proc. Combust. Inst. 35 (2) (2015) 2389–2396, https://doi.org/10.1016/j.proci.2014.06.115.
[3] H. Fatehi, Z.S. Li, X.S. Bai, M. Aldén, Modeling of alkali metal release during biomass pyrolysis, Proc. Combust. Inst. 36 (2) (2017) 2243–2251, https://doi.org/10.1016/j.proci.2016.06.079.
[4] Y. Liu, Z. Wang, J. Xia, L. Vervisch, K. Wan, Y. He, et al., Measurement and kinetics of elemental and atomic potassium release from a burning biomass pellet, Proc. Combust. Inst. 37 (3) (2019) 2681–2688, https://doi.org/10.1016/j.proci.2018.06.042.
[5] Z. Zhang, Q. Song, Z.T. Alwahabi, Q. Yao, G.J. Nathan, Temporal release of potassium from pinewood particles during combustion, Combust. Flame 162 (2) (2015) 496–505, https://doi.org/10.1016/j.combustflame.2014.07.030.
[6] P.J. van Eyk, P.J. Ashman, Z.T. Alwahabi, G.J. Nathan, The release of water-bound and organic sodium from loy yang coal during the combustion of single particles in a flat flame, Combust. Flame 158 (6) (2011) 1181–1192, https://doi.org/10.1016/j.combustflame.2010.10.024.
[7] P.J. van Eyk, P.J. Ashman, Z.T. Alwahabi, G.J. Nathan, Quantitative measurement of atomic sodium in the plume of a single burning coal particle, Combust. Flame 155 (3) (2008) 529–537, https://doi.org/10.1016/j.combustflame.2008.05.012.
[8] J. Zhang, C.L. Han, Z. Yan, The varying characterization of alkali metals (na, k) from coal during the initial stage of coal combustion, Energy Fuels 15 (4) (2001) 786–793.
[9] E. Björkman, B. Strömberg, Release of chlorine from biomass at pyrolysis and gasification conditions1, Energy Fuels 11 (5) (1997) 1026–1032, https://doi.org/10.1021/ef970031o.
[10] Y. Liu, L. Cheng, Y. Zhao, J. Ji, Q. Wang, Z. Luo, et al., Transformation behavior of alkali metals in high-alkali coals, Fuel Process Technol. 169 (2018) 288–294, https://doi.org/10.1016/j.fuproc.2017.09.013.
[11] M.U. Rahim, X. Gao, M. Garcia-Perez, Y. Li, H. Wu, Release of chlorine during mallee bark pyrolysis, Energy Fuels 27 (1) (2013) 310–317, https://doi.org/10.1021/ef3018157.
[12] A. Kosminski, D.P. Ross, J.B. Agnew, Transformations of sodium during gasification of low-rank coal, Fuel Process Technol. 87 (11) (2006) 943–952, https://doi.org/10.1016/j.fuproc.2005.06.006.
[13] S. Lith, P.A. Jensen, F.J. Frandsen, P. Glarborg, Release to the gas phase of inorganic elements during wood combustion, Part 2 Influ. fuel Compos. Energy Fuels 22 (3) (2008).
[14] M.J. Wornat, R.H. Hurt, N.Y.C. Yang, T.J. Headley, Structural and compositional transformations of biomass chars during combustion, Combust. Flame 100 (1–2) (1995) 131–143. ⟨https://go.exlibris.link/sZWW9HzY⟩.
[15] C.Z. Li, C. Sathe, J.R. Kershaw, Y. Pang, Fates and roles of alkali and alkaline earth metals during the pyrolysis of a victorian brown coal, Fuel 79 (3) (2000) 427–438, https://https://doi.org/10.1016/S0016-2361(99)00178-7.
[16] D.M. Quyn, H. Wu, S.P. Bhattacharya, C.Z. Li, Volatilisation and catalytic effects of alkali and alkaline earth metallic species during the pyrolysis and gasification of victorian brown coal. Part ii, Eff. Chem. Form. Valence Fuel 81 (8) (2002) 1033–1039.
[17] J. Liu, X. Yang, X. Jiang, X. Jiang, Pyrolysis mechanisms of coal extracts based on tg-ftir and ReaxFF md study, Fuel Process Technol. 227 (2022), 107124, https://doi.org/10.1016/j.fuproc.2021.107124.
[18] S.G. Chen, R.T. Yang, The active surface species in alkali-catalyzed carbon gasification: phenolate (C-O-M) groups vs clusters (particles), J. Catal. 141 (1) (1993) 102–113, https://doi.org/10.1006/jcat.1993.1122.
[19] Y. Fang, L. Yin, H. Yang, X. Gong, Y. Chen, H. Chen, Catalytic mechanisms of potassium salts on pyrolysis of β-O-4 type lignin model polymer based on DFT study, Proc. Combust. Inst. 38 (3) (2021) 3969–3976, https://doi.org/10.1016/j.proci.2020.07.038.
[20] D. Feng, Q. Shang, H. Dong, Y. Zhang, Z. Wang, D. Li, et al., Catalytic mechanism of Na on coal pyrolysis-derived carbon black formation: experiment and DFT simulation, Fuel Process Technol. 224 (2021), 107011, https://doi.org/10.1016/j.fuproc.2021.107011.
[21] Z. Lei, J. Yan, R. Xie, Z. Yao, C. Xue, Y. Tian, et al., Catalysis mechanism of solution loss reaction of metallurgical coke in blast furnace: experimental and modeling study, Fuel 290 (2021), 120025, https://doi.org/10.1016/j.fuel.2020.120025.
[22] J.P. Mathews, A.L. Chaffee, The molecular representations of coal-a review, Fuel 96 (2012) 1–14, https://doi.org/10.1016/j.fuel.2011.11.025.
[23] X. Zhang, X. Lü, H. Wu, M. Xie, R. Lin, Z. Zhou, Microscopic mechanism for effect of sodium on no heterogeneous reduction by char, J. Fuel Chem. Technol. 48 (6) (2020) 663–673, https://https://doi.org/10.1016/S1872-5813(20)30050-5.
[24] D. Zhao, H. Liu, C. Sun, L. Xu, Q. Cao, DFT study of the catalytic effect of na on the gasification of carbon–co2, Combust. Flame 197 (2018) 471–486, https://doi.org/10.1016/j.combustflame.2018.09.002.
[25] A.C.T. Van Duin, S. Dasgupta, F. Lorant, W.A. Goddard, ReaxFF: a reactive force field for hydrocarbons, J. Phys. Chem. A 105 (41) (2001) 9396–9409.
[26] E. Salmon, A.C.T. van Duin, F. Lorant, P. Marquaire, W.A. Goddard, Thermal decomposition process in algaenan of Botryococcus braunii race l. Part 2: molecular dynamics simulations using the ReaxFF reactive force field, Org. Geochem. 40 (3) (2009) 416–427, https://doi.org/10.1016/j.orggeochem.2008.08.012.
[27] E. Salmon, A.C.T. van Duin, F. Lorant, P. Marquaire, W.A. Goddard, Early maturation processes in coal. Part 2: reactive dynamics simulations using the ReaxFF reactive force field on morwell brown coal structures, Org. Geochem. 40 (12) (2009) 1195–1209, https://doi.org/10.1016/j.orggeochem.2009.09.001.
[28] M. Gao, X. Li, C. Ren, Z. Wang, Y. Pan, L. Guo, Construction of a multicomponent molecular model of fugu coal for ReaxFF-md pyrolysis simulation, Energy Fuels 33 (4) (2019) 2848–2858, https://doi.org/10.1021/acs.energyfuels.8b04434.
[29] D. Hong, X. Guo, Molecular dynamics simulations of zhundong coal pyrolysis using reactive force field, Fuel 210 (2017) 58–66, https://doi.org/10.1016/j.fuel.2017.08.061.
[30] J. Liu, Y. Jiang, W. Yao, X. Jiang, X. Jiang, Molecular characterization of henan anthracite coal, Energy Fuels 33 (7) (2019) 6215–6225, https://doi.org/10.1021/acs.energyfuels.9b01061.
[31] J. Meng, R. Zhong, S. Li, F. Yin, B. Nie, Molecular model construction and study of gas adsorption of zhaozhuang coal, Energy Fuels 32 (9) (2018) 9727–9737, https://doi.org/10.1021/acs.energyfuels.8b01940.
[32] J. Wang, Y. He, H. Li, J. Yu, W. Xie, H. Wei, The molecular structure of inner mongolia lignite utilizing xrd, solid state ^{13}c nmr, hrtem and xps techniques, Fuel 203 (2017) 764–773, https://doi.org/10.1016/j.fuel.2017.05.042.
[33] Q. Zhong, Q. Mao, J. Xiao, A.C.T. van Duin, J.P. Mathews, ReaxFF simulations of petroleum coke sulfur removal mechanisms during pyrolysis and combustion, Combust. Flame 198 (2018) 146–157, https://doi.org/10.1016/j.combustflame.2018.09.005.
[34] S. Chen, J. Ding, G. Li, J. Wang, Y. Tian, Y. Liang, Theoretical study of the formation mechanism of sulfur-containing gases in the co2 gasification of lignite, Fuel 242 (2019) 398–407, https://doi.org/10.1016/j.fuel.2019.01.010.
[35] Y. Liang, F. Wang, H. Zhang, J. Wang, Y. Li, G. Li, A ReaxFF molecular dynamics study on the mechanism of organic sulfur transformation in the hydropyrolysis

process of lignite, Fuel Process Technol. 147 (2016) 32–40, https://doi.org/10.1016/j.fuproc.2015.09.007.
[36] D. Hong, Z. Cao, X. Guo, Effect of calcium on the secondary reactions of tar from zhundong coal pyrolysis: a molecular dynamics simulation using ReaxFF, J. Anal. Appl. Pyrolysis 137 (2019) 246–252, https://doi.org/10.1016/j.jaap.2018.11.033.
[37] B. Wu, X. Guo, X. Qian, B. Liu, Insight into the influence of calcium on the co-pyrolysis of coal and polystyrene, Fuel 329 (2022), 125471, https://doi.org/10.1016/j.fuel.2022.125471.
[38] C. Sun, X. Wei, R. Kang, F. Bin, S. Li, Intrinsic sodium occurrence in zhundong coal: experimental observations and molecular modeling, Fuel 305 (2021), 121491 https://https://doi.org/10.1016/j.fuel.2021.121491.
[39] H.J.C. Berendsen, J.P.M. Postma, W.F. van Gunsteren, A. Dinola, J.R. Haak, Molecular dynamics with coupling to an external bath, J. Chem. Phys. 81 (8) (1984) 3684–3690, https://10.1063/1.448118.
[40] Rüger F., Yakovlev T., Van Philipsen, Van Vuren, Klumpers B. Amsterdam modeling suite.; 2022.
[41] D. Hou, M. Feng, J. Wei, Y. Wang, A.C.T. van Duin, K.H. Luo, A reactive force field molecular dynamics study on the inception mechanism of titanium tetraisopropoxide (ttip) conversion to titanium clusters, Chem. Eng. Sci. 252 (2022), 117496, https://doi.org/10.1016/j.ces.2022.117496.
[42] L.C. Kröger, W.A. Kopp, M. Döntgen, K. Leonhard, Assessing statistical uncertainties of rare events in reactive molecular dynamics simulations, J. Chem. Theory Comput. 13 (9) (2017) 3955–3960, https://doi.org/10.1021/acs.jctc.7b00524.
[43] M. Döntgen, M. Przybylski-Freund, L.C. Kröger, W.A. Kopp, A.E. Ismail, K. Leonhard, Automated discovery of reaction pathways, rate constants, and transition states using reactive molecular dynamics simulations, J. Chem. Theory Comput. 11 (6) (2015) 2517–2524, https://doi.org/10.1021/acs.jctc.5b00201.
[44] Y. Li, G. Li, H. Zhang, J. Wang, A. Li, Y. Liang, ReaxFF study on nitrogen-transfer mechanism in the oxidation process of lignite, Fuel 193 (2017) 331–342, https://doi.org/10.1016/j.fuel.2016.12.081.
[45] H. Liu, J. Liang, R. He, X. Li, M. Zheng, C. Ren, et al., Overall mechanism of jp-10 pyrolysis unraveled by large-scale reactive molecular dynamics simulation, Combust. Flame 237 (2022), 111865, https://doi.org/10.1016/j.combustflame.2021.111865.
[46] Y. Qiu, W. Zhong, Y. Shao, A. Yu, Reactive force field molecular dynamics (ReaxFF md) simulation of coal oxy-fuel combustion, Powder Technol. 361 (2020) 337–348, https://doi.org/10.1016/j.powtec.2019.07.103.
[47] M. Zheng, X. Li, M. Wang, L. Guo, Dynamic profiles of tar products during naomaohu coal pyrolysis revealed by large-scale reactive molecular dynamic simulation, Fuel 253 (2019) 910–920, https://doi.org/10.1016/j.fuel.2019.05.085.
[48] E. Thorin, F.M. Schmidt, Tdlas-based photofragmentation spectroscopy for detection of K and KOH in flames under optically thick conditions, Opt. Lett. 45 (18) (2020) 5230–5233, https://doi.org/10.1364/OL.400614.
[49] E. Thorin, K. Zhang, D. Valiev, F.M. Schmidt, Simultaneous detection of K, KOH, and KCL in flames and released from biomass using photofragmentation tdlas, Opt. Express 29 (26) (2021) 42945, https://doi.org/10.1364/OE.446725.
[50] C. Sathe, Y. Pang, C.Z. Li, Effects of heating rate and ion-exchangeable cations on the pyrolysis yields from a victorian brown coal, Energy Fuels 13 (3) (1999) 748–755.